Examining the power supplied to Earth's dynamo by magnesium precipitation and radiogenic heat production.

Alfred Wilson
School of Earth and Environment, University of Leeds
https://orcid.org/0000-0002-6602-0990
a.j.wilson1@leeds.ac.uk

Monica Pozzo
Department of Earth Sciences, University College London
https://orcid.org/0000-0003-1004-9273
m.pozzo@ucl.ac.uk

Christopher Davies
School of Earth and Environment, University of Leeds
https://orcid.org/0000-0002-1074-3815
C.Davies@leeds.ac.uk

Andrew Walker
Department of Earth Sciences, University of Oxford
https://orcid.org/0000-0003-3121-3255
andrew.walker@earth.ox.ac.uk

Dario Alfè
Department of Earth Sciences, University College London
https://orcid.org/0000-0002-9741-8678
d.alfe@ucl.ac.uk

This is non-peer reviewed preprint submitted to EarthArxiv, also submitted to Physics of Earth and Planetary Interiors for peer review.

Highlights

Examining the power supplied to Earth's dynamo by magnesium precipitation and radiogenic heat production

Alfred J. Wilson, Monica Pozzo, Christopher J. Davies, Andrew M. Walker, Dario Alfè

- Ab initio calculations of MgO and K_2O chemical potentials in liquid iron and silicates provide partition coefficients between Earth's core and mantle
- Ancient core may have dissolved up to 250 ppm of K, if oxygen concentration was less than 13%, which is insufficient to power the ancient geodynamo in a high thermal conductivity core
- Mg precipitation is not able to sustain the ancient geodynamo without combined extraction of multiple light elements from the core

Examining the power supplied to Earth's dynamo by magnesium precipitation and radiogenic heat production

Alfred J. Wilson[a], Monica Pozzo[b,c], Christopher J. Davies[a], Andrew M. Walker[d], Dario Alfè[b,c,e]

[a]*School of Earth and Environment, University of Leeds, Woodhouse, Leeds, LS2 9JT, United Kingdom*
[b]*Department of Earth Sciences, University College London, Gower Street, London, WC1E 6BT, United Kingdom*
[c]*London Centre for Nanotechnology and Thomas Young Centre@UCL, University College London, Gower Street, London, WC1E 6BT, h, United Kingdom*
[d]*Department of Earth Sciences, University of Oxford, South Park Road, Oxford, OX1 3AN, h, United Kingdom*
[e]*Dipartimento di Fisica Ettore Pancini, Universita di Napoli Federico II, Monte S. Angelo, Napoli, I-80126, Italy*

Abstract

We examine magnesium and potassium solubility in liquid Fe mixtures, representative of Earth's core composition, in equilibrium with liquid silicate mixtures representative of an early magma ocean. Our study is based on the calculation of the chemical potentials of MgO and K_2O in both phases, using density functional theory. For MgO, we also study stability against precipitation of the solid phase. We use thermal evolution models of the core and mantle to assess whether either radiogenic heating from ^{40}K decay or Mg precipitation from the liquid core can resolve the new core paradox by powering the geodynamo prior to inner core formation. Our results on K show that concentrations in the core are likely to be small and the effect of ^{40}K decay on the thermal evolution of the core is minimal, making it inca-

pable of sustaining the early geodynamo alone. Our results also predict small concentrations of Mg in the core although these might be sufficient to power the geodynamo prior to inner core formation, depending on the process by which it is transported across the core mantle boundary.
Keywords: new core paradox, thermal evolution, palaeomagnetism, metal-slicate partitioning

1. Introduction

Over the last decade several theoretical (Pozzo et al., 2012; de Koker et al., 2012; Pozzo et al., 2013, 2014; Pourovskii et al., 2020; Zhang et al., 2022; Pozzo et al., 2022) and experimental studies (Gomi et al., 2013; Ohta et al., 2016; Inoue et al., 2020) have suggested that values of the thermal conductivity (κ) of the Earth's core are much higher than previous estimates based on extrapolations (Stacey and Anderson, 2001; Stacey and Loper, 2007). Classical core evolution studies based on cooling and inner-core growth and including high κ values point to a potential power shortage for maintaining the Earth's magnetic field prior to inner-core formation, believed to be around 0.5-1 Gyr ago (Davies, 2015; Labrosse, 2015; Nimmo, 2015a), which is inconsistent with paleomagnetic determinations of a field back to at least 3.5 Ga (e.g. Biggin et al., 2011) but potentially 4 Ga (Tarduno et al., 2015, 2020; Fu et al., 2021; Bono et al., 2022). This incongruity defines the new core paradox. Significant attention has been focused on identifying alternative power sources that can help to sustain the geodynamo prior to inner-core

formation. In this paper we consider two of the prime candidates: heat released from the decay of ^{40}K, and precipitation of magnesium. In both cases the key challenge is to determine elemental partitioning behaviour at conditions at and above core-mantle boundary (CMB) pressure $P \sim 135$ GPa and temperature $T \sim 4000$ K.

Radiogenic heating provides power for magnetic field generation, though it is thermodynamically inefficient compared to the release of latent heat and light elements that accompany inner core growth because the heat is released throughout the core (Nimmo, 2015a). Indeed the more significant effect of radiogenic heating is to reduce the core cooling rate for the same CMB heat flow, which keeps the core cooler for longer and slows inner core growth. The effect depends on the nature and abundance of radiogenic elements in the core. Both uranium and thorium have been proposed to enter the core during its formation (Wohlers and Wood, 2015), but most thermal history studies have focused on potassium (Nimmo et al., 2004). Early experimental investigations at relatively low $P(\sim 1-24)$ GPa and moderate $T(\sim 2000)$ K found that up to a few hundred ppm ^{40}K could enter the core during its formation (Gessmann and Wood, 2002; Murthy et al., 2003) depending on the abundance of O and S in the metal (Bouhifd et al., 2007). However, laser heated diamond anvil cell experiments (Hirao et al., 2006; Watanabe et al., 2014; Blanchard et al., 2017) and ab initio calculations (Xiong et al., 2018) on molten iron alloys at high $P(> 50)$ GPa and $T(> 3500)$ K suggested small concentrations of only 25-40 ppm. Core-mantle evolution models with low κ

included $\sim$ 400 to 800 ppm to help satisfy constraints on mantle cooling, inner core size and continued dynamo generation (Nimmo et al., 2004; Nakagawa and Tackley, 2010). Other models have argued that at least 250 ppm is required to match the present inner core size and maintain dynamo action with high κ (Driscoll and Bercovici, 2014). Additionally, including small ^{40}K concentrations (30 ppm) has been shown to make little difference to the predicted inner core age and ancient core temperature (Pozzo et al., 2022). Whilst these studies cannot be directly compared, it is clear that the effect of heating from ^{40}K can be significant and the concentration in the core is not agreed upon.

A second proposal to address the reduced power supply to the geodynamo is ascribed to light elements such as Mg and Si precipitating out of solution early in the history of the core, releasing power by leaving behind a heavy liquid that sinks and mixes the bulk core (O'Rourke and Stevenson, 2016; Badro et al., 2016; Mittal et al., 2020). We have recently re-examined the case of Si precipitation (Wilson et al., 2022) and so here we focus on Mg. The power provided by Mg precipitation depends on 1) the amount of Mg dissolved in the core during its formation, c^i_{Mg} (where c is mass fraction of solute); 2) the equilibrium concentration of Mg in the core, c^C_{Mg}, and; 3) the rate of Mg precipitation once the equilibrium concentration falls below the concentration of Mg initially dissolved in the core.

The initial core Mg concentration c^i_{Mg} is difficult to estimate because it depends on the manner in which the core formed. A recent review (Davies

and Greenwood, 2023) used the range 0.3-3.6 wt%, where the lower estimates come from single-stage core formation models (O'Rourke and Stevenson, 2016; Helffrich et al., 2020) while the upper bounds were obtained from formation models that included a late high T event such as a giant impact (O'Rourke and Stevenson, 2016; Badro et al., 2016). The equilibrium Mg concentration c^C_{Mg} has been estimated by modelling high T experiments of partitioning between metal and silicate melts, which show a small pressure effect (Badro et al., 2016, 2018; Du et al., 2019) and so MgO precipitation is expected to occur first at the CMB where the core temperature is lowest. However, the uncertainties on both c^i_{Mg} and c^C_{Mg} mean that the onset time for MgO precipitation is poorly known. Indeed, using the c^C_{Mg} from previous studies (Badro et al., 2018; Du et al., 2019), Davies and Greenwood (2023) showed high c^i_{Mg} ($\sim$3.6 wt%) would have allowed precipitation for all temperatures below 6000 K, i.e. over most of Earth's history, while low c^i_{Mg} ($\sim$0.3 wt%) implies that precipitation does not occur for T above the present-day CMB temperature of $\sim$4000 K (Davies et al., 2015), i.e. Mg has never precipitated from the core.

The power provided by Mg precipitation is proportional to dc^i_{Mg}/dT (O'Rourke and Stevenson, 2016). Early studies obtained a strong temperature effect and hence a large dc^i_{Mg}/dT (O'Rourke and Stevenson, 2016); however, they were forced to use a simplified thermodynamic model (in particular with Mg and O activity coefficients set to zero) owing to a lack of experimental data. Subsequent studies employing larger datasets and more detailed

thermodynamic modelling obtained a weaker T dependence and a strong influence of oxygen content in the metal (Badro et al., 2018; Du et al., 2019). A recent review obtained a precipitation rate in the range 0.3–1.5$\times 10^{-5}$ K^{-1} (Davies and Greenwood, 2023) based on the aforementioned thermodynamic models and a range of plausible core and lower mantle chemistry. Compared to the case with no precipitation, the lower rate produced a minor change in inner core age and early core temperature, while the upper rate could double the predicted inner core age and reduce early core temperatures below 5000 K.

In this paper we present new *ab initio* determinations of MgO and K_2O partitioning between liquid metal and both solid and liquid silicate at CMB conditions, complementing experimental studies that generally access lower PT. We employ our recently developed methodology for computing chemical potentials, which gives good agreement with extrapolations based on experimental determinations of FeO (Pozzo et al., 2019) and SiO_2 (Wilson et al., 2022) partitioning. We model Fe-rich metallic liquid alloyed with O and Si, since these lighter elements are generally predicted to be incorporated into the early core (Rubie et al., 2015; Badro et al., 2015) and can satisfy the present-day core mass and inner core boundary density jump (Davies et al., 2015). Reasonable compositions which are consistent with seismic observation contain up to 15 mol. % O (Badro et al., 2015; Davies and Greenwood, 2023). We include a silicate melt as representative of the early mantle, when thermal history models predict CMB temperatures far above the pyrolite

solidus (Nimmo, 2015b; Davies et al., 2015). We compare our results to literature data and incorporate them into core evolution models to predict the viability of dynamo action over geological time and to constrain the age of the inner core.

2. Methods

Partitioning of elements between the core and mantle is represented here by the partition coefficient of a species between silicate and iron-rich liquid. These coefficients are calculated from the difference of chemical potential of the species in each system which in turn are evaluated via free energies in ab initio molecular dynamic calculations. In this section we describe the theory of chemical equilibrium and the partition coefficients which form the basis of this work, as well as how these are calculated from first principles using chemical potentials.

2.1. Chemical equilibrium

Chemical equilibrium is reached when the chemical potentials μ of all species are equal in the liquid iron mixture and the liquid silicate. Experiments usually report distribution of composite species in the silicate, such as FeO, SiO_2, MgO and K_2O, and so the relevant equations are, for example for K_2O and MgO:

$$\mu^C_{\mathrm{K_2O}}(p, T, x^C_i, x^C_j, \dots) = \mu^{\mathrm{M}}_{\mathrm{K_2O}}(p, T, x^{\mathrm{M}}_i, x^{\mathrm{M}}_j, \dots), \tag{1}$$

$$\mu^C_{\rm MgO}(p,T,x^C_i,x^C_j,\dots) = \mu^{\rm M}_{\rm MgO}(p,T,x^{\rm M}_i,x^{\rm M}_j,\dots), \tag{2}$$

where $x^C_i, x^C_j, \dots$ are the molar concentrations of elements $i, j, \dots$ in the core (superscript C) and mantle (superscript M). For simplicity of notation in the following we will leave out explicitly writing the dependence of μ on $p, T, x_i, x_j, \dots$. If the composite species are dissolved into their respective systems, then Eq. 1 and 2 can be written in terms of the chemical potentials of the single elements:

$$\mu^M_{K_2O} = \mu^C_{K_2O} = 2\mu^M_K + \mu^M_O, \tag{3}$$

$$\mu^M_{MgO} = \mu^C_{MgO} = \mu^M_M g + \mu^M_O. \tag{4}$$

This is indeed the case for the liquid iron mixture, and to some extent also for the liquid silicate where individual elements can be present in multiple species.

To obtain the relation that governs partitions it is useful to re-write the chemical potential by separating the configurational part and so Eq. 1 for K_2O becomes

$$2[k_{\rm B}T\ln x^C_{\rm K}+\tilde{\mu}^C_{\rm K}]+k_{\rm B}T\ln x^C_{\rm O}+\tilde{\mu}^C_{\rm O} = 2[k_{\rm B}T\ln x^{\rm M}_{\rm K}+\tilde{\mu}^{\rm M}_{\rm K}]+k_{\rm B}T\ln x^{\rm M}_{\rm O}+\tilde{\mu}^{\rm M}_{\rm O}, \tag{5}$$

and similarly for MgO. Eq. 5 can be rearranged in terms of the partition

coefficients:

$$K_D^K = \frac{(x_{\mathrm{K}}^C)^2 x_{\mathrm{O}}^C}{(x_{\mathrm{K}}^{\mathrm{M}})^2 x_{\mathrm{O}}^{\mathrm{M}}} = \exp\left(-\frac{\tilde{\mu}_{\mathrm{K_2O}}^C - \tilde{\mu}_{\mathrm{K_2O}}^{\mathrm{M}}}{k_{\mathrm{B}}T}\right) = \exp\left(-\frac{\delta\tilde{\mu}_{\mathrm{K_2O}}}{k_{\mathrm{B}}T}\right), \qquad (6)$$

where $\tilde{\mu}^{\mathrm{K_2O}} = 2\tilde{\mu}^{\mathrm{K}} + \tilde{\mu}^{\mathrm{O}}$ for the liquid metal and liquid silicate. For MgO we obtain

$$K_D^{Mg} = \frac{x_{\mathrm{Mg}}^C x_{\mathrm{O}}^C}{x_{\mathrm{Mg}}^{\mathrm{M}} x_{\mathrm{O}}^{\mathrm{M}}} = \exp\left(-\frac{\tilde{\mu}_{\mathrm{MgO}}^C - \tilde{\mu}_{\mathrm{MgO}}^{\mathrm{M}}}{k_{\mathrm{B}}T}\right) = \exp\left(-\frac{\delta\tilde{\mu}_{\mathrm{MgO}}}{k_{\mathrm{B}}T}\right). \qquad (7)$$

Complete details of the approach we outline here are given by Pozzo et al. (2019). μ_X is calculated via several different computational methods, all based on thermodynamic integration. Here, we use two of these approaches, referring to them henceforth as *Method 1* and *Method 2*. In *Method 1*, a system A is *slowly* transformed (that is, allowing the system to remain in thermodynamic equilibrium) into system B, and the reversible work performed in this *alchemical* transmutation is equal to the free energy difference between B and A. This transformation involves changing the number of solute units in the system, meaning the change in free energy is equal to $\tilde{\mu}$ of the solute. *Method 2*, also described in Pozzo et al. (2019), is to refer to an external potential of known free energy, both for system A and system B. The transmutations from the external potential to the ab-initio potential then gives access to the total free energies of A and B, and from their difference one can obtain once again the chemical potential of interest. These two approaches are completely independent from one another, and by applying

them both we can double check the internal consistency of our results and quantify uncertainty of the overall method.

We also calculate K_D^{Mg} between the liquid core and solid B1 structure MgO at the centre of the Earth. This provides an additional test of our method and helps to determine the process of Mg exsolution from the liquid core. This requires a slightly different approach to the other solutes in the core and an adjustment to the methods laid out by Pozzo et al. (2019). We used *Method 1*, in which the reference potential is the harmonic system, obtained by expanding the DFT potential energy function as function of atomic displacements from their equilibrium zero temperature positions, and including only the quadratic term in the expansion:

$$U_{\mathrm{h}}(\mathbf{R}) = U_0 + \sum_{i,j;i<j} \mathbf{u}_i \cdot \Phi_{ij} \cdot \mathbf{u}_j, \tag{8}$$

where $U_h\left(\mathbf{R}\right)$ is the total harmonic energy function of the system which depends on the positions ($\mathbf{R} = \mathbf{r_1}, \ldots \mathbf{r_N}$) of all the atoms. $\mathbf{u}_i = \mathbf{r}_i - \mathbf{r}_i^0$ is the displacement of atom i from its zero temperature equilibrium position $\mathbf{r}_i^0$, U_0 the value of the potential with zero displacements, and $\Phi_{ij} = \frac{\partial^2 U}{\partial \mathbf{r}_i^0 \partial \mathbf{r}_j^0}$ the *force constant matrix*, with the derivatives calculated at the equilibrium positions. The force constant matrix is computed using the small displacement method, as implemented in the PHON code (Alfè, 2009). The free energy per formula unit of MgO of the harmonic system U_{ref} is obtained by summing

the contributions of each normal mode $\omega_{\mathbf{q},s}$:

$$F_h(T) = k_{\mathrm{B}}T\frac{1}{N_{\mathbf{q}}}\sum_{\mathbf{q}}\sum_{s}\ln\left\{2\sinh\frac{\hbar\omega_{\mathbf{q},s}}{2k_{\mathrm{B}}T}\right\}, \tag{9}$$

where $\hbar$ is the reduced Plank's constant, $\sum_s$ runs over the 6 phonon branches (3 acoustic and 3 optical in the MgO crystal), and $\frac{1}{N_{\mathbf{q}}}\sum_{\mathbf{q}}$ is used to approximate the integral over all wavevectors $\mathbf{q}$ in the Brillouin Zone. The latter sum usually converges very quickly w.r.t. the number of $\mathbf{q}$ included and it is straightforward to compute once the force constant matrix is known. In fact, since the chemical potential of MgO in the liquid core is calculated by assuming that the atomic nuclei behave classically, we use the classical approximation for the harmonic free energy, given by:

$$F_h^C(T) = k_{\mathrm{B}}T\frac{1}{N_{\mathbf{q}}}\sum_{\mathbf{q}}\sum_{s}\ln\left\{\frac{\hbar\omega_{\mathbf{q},s}}{k_{\mathrm{B}}T}\right\}. \tag{10}$$

We note that at the conditions of interest the difference between the classical approximation and the full quantum free energy is only $\sim$ 4-5 meV/formula unit, which is negligible for all practical purposes. By using the classical approximation for the solid as well as the liquid errors are minimised.

2.2. Ab initio simulations

The calculations are based on density functional theory (Hohenberg and Kohn, 1964; Kohn and Sham, 1965), using the VASP code (Kresse and Furthmüller, 1996), with the projector augmented wave (PAW) method (Blöchl,

	Fe	K	Si	Mg	O
PAW core	[Ne]$3s^2$	[Ne]	[Ne]	[He]	[He]
Valence electrons	14	9	4	8	6
Core radii (Å)	1.16	1.22	0.79	1.06	0.80

Table 1: Electronic configurations and core radii of the PAW potentials employed in this work.

1994; Kresse and Joubert, 1999) and the generalised gradient corrected functional known as PW91 (Wang and Perdew, 1991). Single particle wavefunctions were expanded in plane waves, with an energy cutoff of 500 eV. The electronic configuration of the various elements and the core radii are detailed in table 2.2.

Electronic levels were occupied according to Fermi-Dirac statistics, with an electronic temperature equal to the ionic temperature. An efficient extrapolation of the charge density was used to speed up the ab initio molecular dynamics (AIMD) simulations (Alfe, 1999), which were performed by sampling the Brillouin Zone (BZ) with the Γ point only. The temperature was controlled with a Nosé thermostat (Nosé, 1984) and the time step was set to 1 fs. The simulation cells contained between 148 and 160 atoms in total, depending on composition.

3. Results

We calculate the chemical potentials of MgO and K_2O in the magma ocean and in the liquid core. For convenience in our calculations, we set the composition of the mixtures at the outset, and then subtract a number

of molecules dN. As a result, the compositions of the liquids are slightly different in the various cases, which could result in small differences in the chemical potentials if they depend on concentration. However, within the statistical accuracy of our calculations we cannot detect any such dependency. These chemical potentials are used to calculate the partition coefficients of Mg and K at the CMB, which will set the equilibrium composition of the core at the CMB.

Our calculations are carried out at pressures relevant to the CMB (124 GPa) as well as at mid-mantle pressures to examine the effect of pressure on K_D. We run the majority our simulations at 5500 K to emulate the conditions of the hot early core, as these are more important for the thermo-chemical evolution of the core than the lower temperatures of the present day CMB (Davies and Greenwood, 2023). K_D at these temperatures can be extrapolated to lower temperatures using the heat of reaction, also calculated here. We also include a low temperature (3600 K) result to better examine the T dependence of K_D. We study a silicate composition which is close to pyrolitic (43.75 mol. % MgO, 6.25 mol. % FeO, 50 mol.% SiO_2) and an additional case representing a more reduced case (55 mol. % MgO, 16 mol. % FeO, 29 mol. % SiO_2). The metal compositions are chosen to explore reasonable O (4-16 mol. %) and Si (0-8 mol. %) concentrations, and an extreme case to better understand the role of O in the metal.

Table 2: Ab initio excess chemical potential differences $\delta\tilde{\mu}_X$ (eV) between the metal and the silicate phases for various compositions, pressures and temperatures. Also reported are the difference in the heat of reactions δH_X (eV) and the partition coefficients K_D.

Species	Metal composition	Silicate composition	p GPa	T K	$\delta\tilde{\mu}_X$ eV	δH_X eV	K_D
MgO	$Fe_{147}O_6$	$Mg_{28}Fe_4Si_{32}O_{96}$	124	5500	3.25(33)	6.47(45)	$0.001^{+0.001}_{-0.0005}$
K_2O	$Fe_{147}O_6$	$Mg_{28}Fe_4Si_{32}O_{96}$	124	5500	5.86(16)	9.24(1.1)	$\leq 10^{-5}$
MgO	$Fe_{121}Si_{12}O_{20}$	$Mg_{28}Fe_4Si_{32}O_{96}$	124	5500	2.62(13)	4.96(16)	$0.004^{+0.001}_{-0.001}$
K_2O	$Fe_{121}Si_{12}O_{20}$	$Mg_{28}Fe_4Si_{32}O_{96}$	124	5500	5.29(17)	7.22(5)	$\leq 2 \times 10^{-5}$
MgO	$Fe_{107}O_{46}$	$Mg_{28}Fe_4Si_{32}O_{96}$	124	5500	1.54(13)	2.50(73)	$0.039^{+0.012}_{-0.010}$
K_2O	$Fe_{107}O_{46}$	$Mg_{28}Fe_4Si_{32}O_{96}$	124	5500	2.41(17)	3.48(43)	$0.006^{+0.003}_{-0.002}$
MgO	$Fe_{125}Si_6Mg_3O_{25}$	$Mg_{38}Fe_{11}Si_{20}O_{91}$	58	3600	1.66(9)	0.38(96)	$4.7^{+1.6}_{-0.8} \times 10^{-3}$
MgO	$Fe_{147}O_6$	$Mg_{28}Fe_4Si_{32}O_{96}$	50	5500	3.22(27)	4.39(53)	$1.0^{+1.0}_{-0.5} \times 10^{-3}$

3.1. Magnesium

In table 2 we report excess chemical potential differences $\delta\tilde{\mu}_{MgO}$ between the core and the silicate mixtures containing Mg, as well as the resulting partition coefficients K_D^{Mg}, and the differences in the heat of reactions δH_{MgO}. We complete some calculations using both *Method 1* and *Method 2* described in section 2. The two approaches show good internal consistency, and therefore for each species we take the weighted averages as our final results, with weights given by the inverse of the squares of the standard deviations. Low values of K_D^{Mg} for MgO are consistent with previous works (Wahl and Militzer, 2015) and imply low solubility of Mg in iron rich alloys, consistent with experimental studies (e.g. Badro et al., 2016, 2018; Chidester et al., 2017; Du et al., 2017; Jackson et al., 2018). Details of separate metal and silicate calculations can be found in the supplementary information.

We compare predicted magnesium partitioning at the CMB from our results with the experimental data. The transfer of Mg can be represented using two possible reactions that can represent the rensfer of Mg are dissociation (dc) and dissolution (dl). These reactions are written respectively as

$$\mathrm{MgO^M} \Longleftrightarrow \mathrm{Mg^C} + \mathrm{O^C}, \tag{11}$$

$$\mathrm{MgO^M} \Longleftrightarrow \mathrm{MgO^C}. \tag{12}$$

The equations determining the partition coefficients K_D^i for reaction i are

$$\log K_D^{dc} = \log \frac{x_{Mg}^C x_O^C}{x_{MgO}^M} = a + \frac{b}{T} + c\frac{P}{T} - \log \gamma_{Mg} - \log \gamma_O. \tag{13}$$

$$\log K_D^{dl} = \log \frac{x_{MgO}^C}{x_{MgO}^M} = a + \frac{b}{T} + c\frac{P}{T} - \log \gamma_{Mg} - \log \gamma_O, \tag{14}$$

Here x_i is the molar concentration of species i, γ_i the activity coefficient, and a, b and c are coefficients that are fixed by fitting to experimental data. γ_i account for compositional variation in K_D meaning that for the ideal case, $\gamma_i = 1$. Note that the activity coefficients in the dissolution reaction arise because it is assumed that dissolved MgO further breaks down into Mg and O (Badro et al., 2018), while silicate activities are set to 1.

Figure 1 compares the Mg partition coefficients in table 2 to literature data, where because MgO is expected to break down to ionic species in the dissolution case, our K_D^{dl} and K_D^{ds} are equal. We use the dataset and

thermodynamic modelling approach from Badro et al. (2018). Briefly, the model uses the interaction parameter formulation of Ma (2001) to represent the compositional dependence of K_D and considers interactions between Fe, O, Si, Mg, C, and S. In the figure, red points show the data assuming no compositional dependence (activity coefficients set to 1), white points show K_D with $\gamma_i \neq 0$, and squares show our data (lines show K_D^{Mg} projected by $\pm$500 K based on the local derivatives of the chemical potential).

We find a strong T and weak P dependence of K_D, in agreement with previous studies (e.g. Fischer et al., 2015; Badro et al., 2018). As in Du et al. (2019), $\log K_D$ increases with increasing oxygen concentration in the metal. Our largest O concentration is 30 mol% while our smallest O concentration is 4 mol%, which encompass the values in the Badro et al. (2018) database. The variation in K_D over this range of O from Du et al. (2019) is around 2 log units, similar to our findings. We find P dependence to be small, which is consistent past studies (e.g. Badro et al., 2018; Du et al., 2019).

By comparing fits of partitioning data to the predictions from Eq.s 13-14 it is hopefully possible to elucidate a single underlying reaction and use this to estimate the equilibrium Mg concentration at the CMB. Badro et al. (2018) found that these two reactions gave comparable fits to their dataset, but favoured the dissolution model as it produced less scatter at high Mg and O metal concentrations. Badro et al. (2018) also examined the exchange reaction but found it inferior to the other reactions, so we do not consider it here. For the dissociation reaction our K_D^{Mg} values bracket the experimental

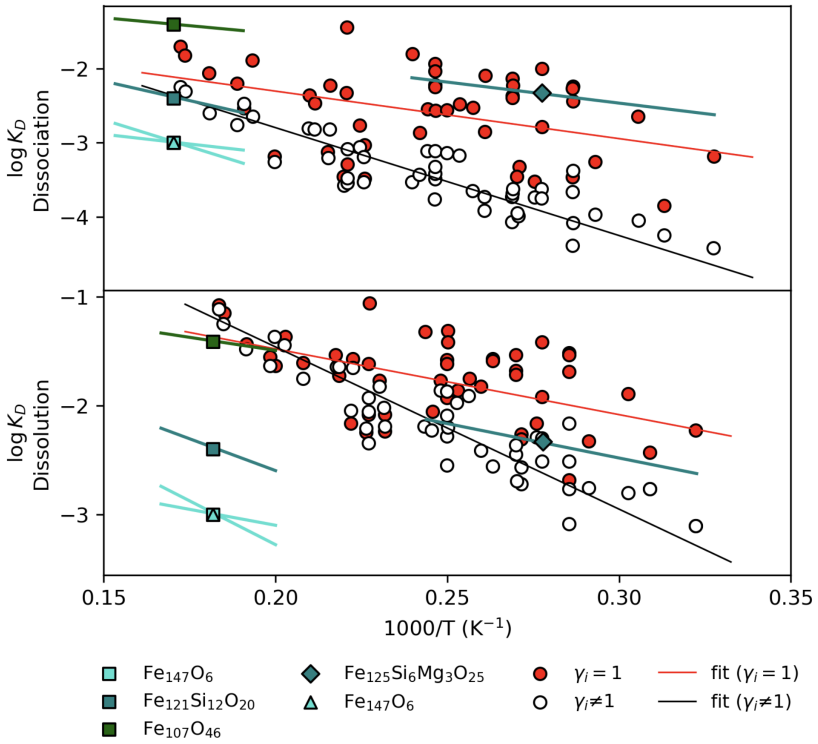

Figure 1: Temperature dependence of MgO partition coefficients for dissociation (top) and dissolution (bottom) reactions. Our results explore four oxygen concentration; 4 mol. % (turquoise), 13-15 mol. % (teal), 30 mol. % (green), and three pressures; 124 GPa (squares), 58 GPa (diamond), 50 GPa (triangle)). Lines show extrapolation of our results via $\frac{\delta \mu_x}{\delta T} = \frac{\mu_x - H_x}{T}$ for ± 500 K. The dataset and model of Badro et al. (2018) are used for experimental ideal $\gamma_i = 1$ (red points) and non-ideal $\gamma_i \neq 1$ (white points), where compositional effects are included. Fits of ideal and non-ideal K_D are shown as read and black lines respectively.

dataset at high T, while for the dissolution reaction our $x_O^C < 30$ mol. % results lies below the experimental range at high T. We therefore favour the dissociation reaction over dissolution.

We also calculate K_D^{Mg} for MgO between the liquid core and solid B1 MgO to further test our ab initio methods and provide a more complete picture of how Mg is exsolved from the liquid core. Results, reported in table 3, agree qualitatively with Wahl and Militzer (2015), showing that only a very small amount of B1 MgO would be stable in solution in the liquid core, against precipitation of its solid phase. K_D is smaller here than for the lower P and T liquid silicate interaction. This is largely because of the limited configurational space in the solid B1 structure compared to the liquid silicate. The T dependence of solubility means that exsolution of Mg will occur at the coldest region of the core first, but these results also show that solid precipitate would not be stable deep in the core either. Precipitation of Mg must therefore occur at the CMB where metal-silicate interaction is present.

3.2. Potassium

Due to a lack of experimental partitioning data for K at high pressure and temperature, it is not possible to effectively compare different reaction types as we have done with Mg. We only consider the dissociation reaction,

$$K_D^K = \frac{{x_K^C}^2 x_O^C}{x_{K_2O}^M}, \tag{15}$$

Table 3: Excess chemical potential differences $\delta\tilde{\mu}_{\mathrm{MgO}}$ (eV) for MgO between liquid iron with various compositions and the solid B1 structure. Calculations have been performed with *Method 1* [*Method 2*] for the liquid, and with *Method 1* for the solid, using the inverse power and the harmonic potential as reference systems, respectively. Also reported are the difference in the heat of reaction δH_{MgO} (eV), $\frac{\partial\delta\tilde{\mu}_{\mathrm{MgO}}}{\partial p}$ (eV/GPa), $\frac{\partial\delta\tilde{\mu}_{\mathrm{MgO}}}{\partial T}$ (eV/1000 K) and the partition coefficient K_D^{Mg}.

Liquid composition	$\frac{\partial\delta\tilde{\mu}_{\mathrm{MgO}}}{\partial p}$	$\frac{\partial\delta\tilde{\mu}_{\mathrm{MgO}}}{\partial T}$	P GPa	T K	$\delta\tilde{\mu}_{\mathrm{MgO}}$ eV	δH_{MgO} eV	K_D^{Mg}
$Fe_{147}O_6$	0.0023(7)	-0.42(13)	364	6500	5.08(7) [5.04(9)]	7.82(83)	$1.2^{+0.1}_{-0.2} \times 10^{-4}$
$Fe_{107}O_{46}$	0.0016(4)	-0.07(8)	364	6500	3.30(14)	3.74(52)	$2.8^{+0.8}_{-0.7} \times 10^{-3}$
$Fe_{121}Si_{12}O_{20}$	0.0007(5)	-0.12(7)	364	6500	4.16(15)	4.97(77)	$5.9^{+1.8}_{-1.3} \times 10^{-4}$
$Fe_{147}O_6$	0.0074(6)	-0.34(11)	135	4500	4.76(6)	6.27(50)	$4.7^{+0.8}_{-0.7} \times 10^{-6}$

due to compatibility with the ionic nature of liquid metals, minimal assumptions compared to other reactions (exchange implies a certainty of FeO exchange coupled to K_2O, excluding the possibility of other candidates) and successful implementation in other systems (e.g. Mg and Si; Wilson et al., 2022).

Our calculations show small K_D^K for K_2O at all conditions studied (see table 2), consistent with previous theoretical and experimental studies (Xiong et al., 2018; Gessmann and Wood, 2002; Hirao et al., 2006; Bouhifd et al., 2007; Blanchard et al., 2017). Figure 2 compares K_D^K from experiment with our results and illustrates that solubility is not dependent on O concentration for reasonable values.

Xiong et al. (2018) find that for a liquid outer core with 23 mol. % O at 4000 K only 30 ppm of K would be soluble in the core, or perhaps as low

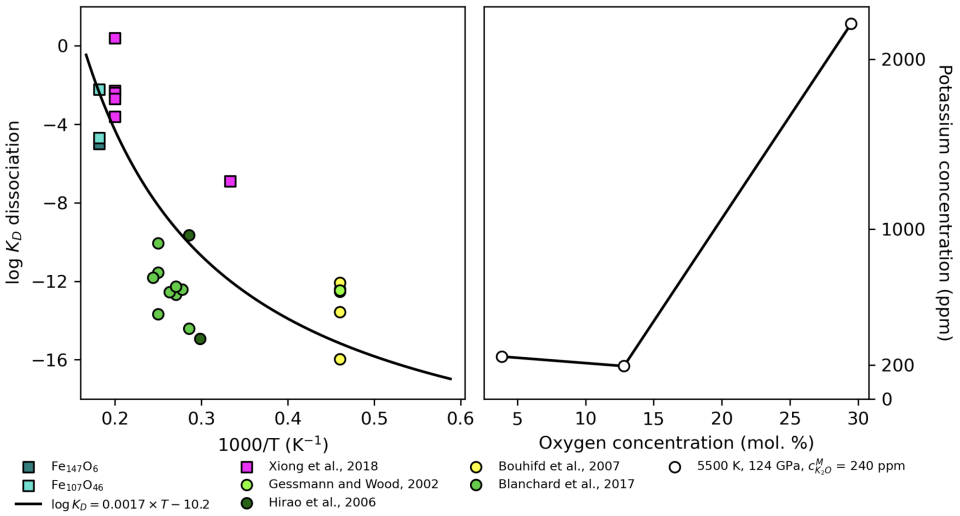

Figure 2: Left: Potassium partition coefficient as a function of the inverse of temperature from this study (teal and turquoise squares) compared with another ab initio study (pink squares; Xiong et al., 2018) and several experimental partitioning studies (circles; Gessmann and Wood, 2002; Hirao et al., 2006; Bouhifd et al., 2007; Blanchard et al., 2017). Experimental K_D^K is calculated from element concentrations in recovered quenched samples (Eq. 15). Black line is the best-fit of temperature dependence $\log K_D^K = A * T + B$. Right: compositional dependence of K solubility in the core, where K is assumed to enter the core through dissociation.

as 1 ppm, amounting to a negligible radiogenic contribution to core power sources. We note that a different formulation of K_D^K is used in this study and our results would also predict 1-30 ppm equilibrium concentration of K in the core given this formulation, instead we simply consider a dissociation reaction (Eq. 15). Our calculations suggest a $K_D^K = 1\times10^{-5}-6\times10^{-3}$ and a significant oxygen dependence above 13 mol. % (fig. 2). For a primitive mantle with a K concentration of 240 ppm (McDonough and Sun, 1995), increasing core oxygen concentration from 3 to 30 mol % promotes K solubility by ∼10x from 250 to 2200 ppm. Despite the elevated solubility, this demonstrates that even for all but unrealistic compositions (30 mol% O) the maximum concentration of K in the core is small.

4. Discussion

To examine the effect of MgO and K_2O on the power available to the ancient geodynamo in a high k core, we simulate the thermal history of the deep Earth whilst varying these contributions. We use a thermodynamic model of Mg solubility to define precipitation of light elements from the liquid core. The removal of these light elements at the CMB leaves an iron-rich density anomaly at the top of the liquid core which provides additional convective power. For K, we use our results to define the temperature dependence of solubility and set initial core compositions. The decay of ^{40}K then heats the core, helping to offset the greater conductive power loss in a high k scenario.

4.1. MgO

Thermal histories of the Earth's core are modelled using coupled 1D parameterisations of the core (Greenwood et al., 2021) and mantle (Driscoll and Bercovici, 2014). These models are joined at the CMB where the mantle defines the heat flux out of the core and the core defines the CMB temperature. Thermal conductivity is 70 W m^{-1} K^{-1} everywhere in the core to represent a moderately high thermal conductivity scenario (Davies and Greenwood, 2023). To assess the power available to the geodynamo E_j, the core entropy is balanced (whilst ignoring small terms) by

$$E_j + E_k = E_s + E_L + E_g + E_{ppt}. \tag{16}$$

Here E_k is the heat conducted out of the core, E_s is the secular heat stored in the core, E_L is the latent heat release due to IC growth and E_g is the gravitational power generated from the preferential partitioning of O into the lowermost liquid core upon freezing. Additional entropy is produced in the liquid core from the precipitation of Mg at the CMB

$$E_{ppt} = \frac{1}{T_{cmb}} \int_{\infty} \psi \rho \alpha_{ppt}^{Mg} \left[C^{Mg} \left(\frac{dT_{cmb}}{dt} \right) \right] dV_c \tag{17}$$

where T_{cmb} is T at the CMB, V_c is the volume of the core, ψ is gravitational potential, ρ is density, $C^{Mg} = \frac{dc_{Mg}^{C}}{dT_{cmb}}$ is the precipitation rate of Mg (in wt. % K^{-1}), and chemical expansivity is $\alpha_{ppt}^{Mg} = 1.12$ (O'Rourke and Stevenson, 2016). Precipitation is quantified by removing Mg from the core until the

equilibrium concentration at the CMB is achieved. This assumes that the core is thoroughly mixed on timescales far shorter than the cooling rate and that precipitation occurs at the coolest part of the core. We treat the mantle which interacts with the core as a constant composition, equal to the bulk composition, meaning that the mantle similarly sweeps precipitate from the CMB on timescales shorter than the cooling rate and that the volume of the mantle is sufficiently large that the precipitate will make little difference to the bulk composition.

To define the equilibrium concentration of Mg in the core, we use the interaction parameter model of Ma (2001) with the parameters found by Badro et al. (2018), who also studied this problem but inferred thermal evolution outcomes from their own temperature dependence of solubility and the core cooling rate of O'Rourke et al. (2017). This model is based on liquid-liquid interaction between metal and silicate. Whilst our thermal evolution model does not include a liquid mantle, this is preferable to any of the alternative models, which include such layers, because of the various highly uncertain parameters which are required to define them. We set initial compositions for the core and mantle for each case and tune models to satisfy present day constraints of heat flux from the convecting mantle (38 TW, Jaupart et al., 2007), min-mantle temperature (Katsura et al., 2010, 2320 K,) and inner core radius (1221 km) and maintaining positive entropy for powering the geodynamo during the last 3.5 Gyrs. We vary the initial CMB temperature (T_{cmb}) and ratio of upper to lower mantle viscosity ($f_{viscosity}$) where the cooling rate

of the core is tuned by $f_{viscosity}$ and the initial temperature of the core is set by T_{cmb}.

We consider two precipitation scenarios and three different initial compositions for each of the mantle and the core. The precipitation scenarios explore how Mg is removed from the core. In the first scenario, Mg and O are removed to the mantle in equal proportion as Mg is precipitated, ensuring charge balance and also reducing the melting point depression associated with O content of the core. In the second scenario, only Mg is removed, accounting for the possibility that other reactions may account for charge balancing. Our calculations do not define what is precipitating from the core, only the stable fraction of Mg in the liquid metal. These two scenarios explore the uncertainty of how Mg is transported across the CMB whilst also examining the extremes of E_{ppt}. When removing Mg and O from the core through Mg precipitation, significantly more convective power is contributed to the core because far more mass is being transfered across the CMB.

We consider a mantle composition of 30, 50 (pyrolitic) and 70 mol. % MgO, where higher concentrations allow more Mg to be dissolved into the core (Eq. 7). We also consider three initial oxygen concentrations of the core (5, 10 and 20 mol. %). The model of Badro et al. (2018) predicts that Mg and O are mutually beneficial for solubility in the core, meaning a more oxidised core can host higher Mg concentrations and therefore provide more power from precipitation. The initial Mg concentration of the core is the equilibrium concentration at the CMB for the initial conditions for our cases.

A maximum of 2 mol.% Mg is dissolved into the core (for a 20 mol.% O in the core and 70 mol.% MgO in the mantle) and a minimum of 0.4 mol.% (5 mol.% O and 30 mol.% MgO). These core and mantle compositions represent a reasonable range as lower concentrations result in limited Mg being dissolved into the core at early times, and therefore limited power from precipitation immediately before inner core nucleation. Higher O concentrations produce significant melting point depression of the iron alloy in the core, meaning that for the core to be cold enough to freeze the inner core, the core becomes too cold.

We evolve these nine starting compositions and two precipitation scenarios both with ($Q_{ppt} \neq 0$) and without ($Q_{ppt} = 0$) the power from precipitation included, giving thirty six individual models. In each case we tune $f_{viscosity}$ and T_{cmb} to best fit the present day constraints. If a case is unable to maintain $E_j > 0$ for all time after 3.5 Ga, it is possible to increase the available entropy, for example through a hotter initial T_{cmb}, however this will result in a smaller than observed present day inner core. All cases presented here have been tuned to best match present day constraints and whilst some may fail by a small margin, this represents the most optimised case. Figure 3 shows example cases where an initial core O concentration of 10 mol. % and pyrolitic mantle is evolved with just Mg being extracted and with Mg precipitation also removing O to maintain charge balance. These cases illustrate the additional convective power supplied by the precipitation of MgO over Mg. At the time when the inner core forms, precipitation of Mg is slow, meaning

that for both cases there is little difference in the rate of change of O concentration because this is controlled predominately by inner core growth. The inner core age does not differ greatly between these two cases, highlighting that whilst Q_{ppt} can be small, the effect of E_{ppt} remains significant.

All models where $Q_{ppt} = 0$ fail to maintain $E_j > 0$ prior to inner core nucleation (O'Rourke et al., 2017; Driscoll and Davies, 2023). Similarly, all models where only Mg is extracted through precipitation (O concentration only changes due to inner core growth) also fail in this regard. All models where both Mg and O are removed from the liquid core with cooling are able to maintain surplus power for the geodynamo for all time after 3.5 Ga but those with an initial O concentration of 20 mol. % struggle to reproduce a present day mantle temperature. Figure 4 compares the age of the inner core and the CMB temperature at 3.5 Ga (indicative of early core conditions) for these successful cases. The high temperatures of the early core are consistent with the temperatures our ab inito calculations were performed at and suggest that liquid-liquid interactions at the CMB were long lived. O content of the core provides a strong control on the core temperature due to melting point depression of the iron alloy; more O rich models must be cooler in order to freeze the inner core. When the mantle contains less MgO compared to pyrolite, or the O concentration of the core is lower, there is less Mg dissolved into the core and precipitation rates are lower. For E_j to be greater than zero prior to inner core formation, these cases must extract slightly more heat through secular cooling meaning that the inner core is older by 20-50 Myrs.

The opposite is true, to a lesser degree for mantle compositions with more MgO than pyrolite, producing elevated precipitation rates. These differences are relatively small, meaning that ancient core temperatures are similar.

4.2. Potassium

We apply the same model as detailed above for studying the effect of ^{40}K on the thermal evolution of the core, except without the precipitation of MgO and with the heat from ^{40}K decay. There are relatively few experimental metal-silicate partitioning studies which include K compared with those including Mg (due to ubiquity in silicates). This, combined with the low solubility of K in liquid Fe, makes the construction of a thermodynamic model (such as those by Badro et al., 2018; Wilson et al., 2022) challenging. Parameters defining the various possible interactions of potassium in iron rich liquids are not yet resolvable. As such we are unable, with presently available experimental data, to construct a thermodynamic partitioning model for K of any utility. Instead we define the temperature dependent solubility of K in the core completely with our own calculated K_D^K (table 2). We find that decay rate exceeds the exsolution rate due to core cooling in all cases meaning that we do not include a temperature dependence of solubility and simply set an initial K concentration for the core.

We produce three cases of initial concentrations of ^{40}K; 0 ppm as a reference, 100 ppm as a low concentration, 250 ppm as the maximum soluble concentration allowed by our K_D^K with reasonable O concentrations (e.g.

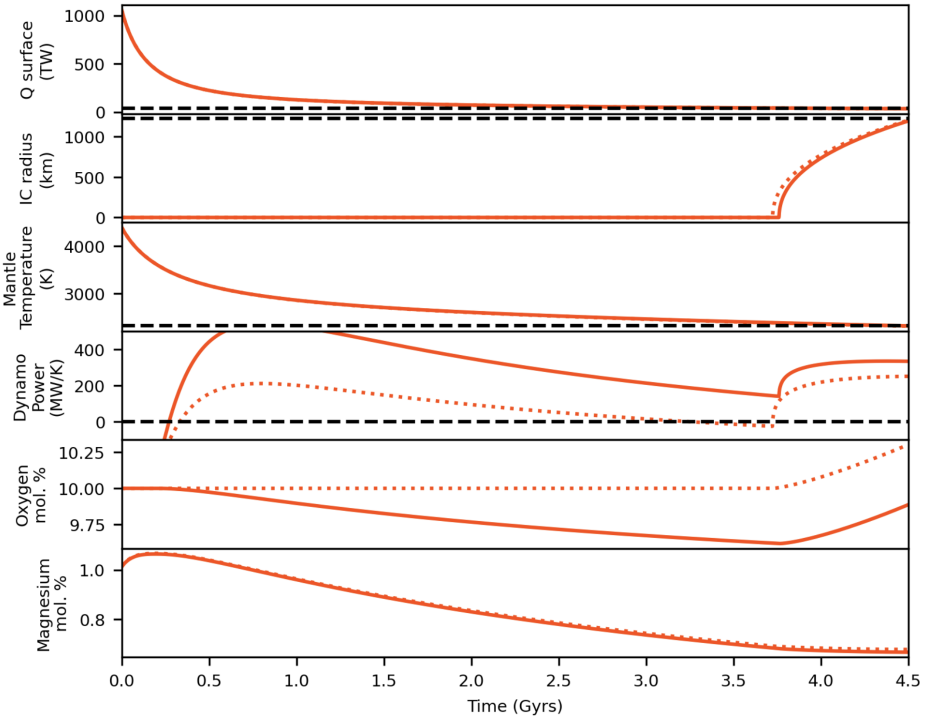

Figure 3: Thermal histories including the precipitation of Mg from the core. Successful models are those which reproduce properties of the deep Earth (black dashed lines; surface heat flow, inner core size and mid-mantle temperature) whilst consistently providing power for the geodynamo ($E_j > 0$). Example cases are shown for a pyrolitic mantle and a 10 mol. % initial oxygen content of the core. When O and Mg are extracted in equal proportion to the mantle via precipitation of Mg (solid lines), each contribute similar convective power to the outer core and $E_j > 0$ for all time. When only Mg is removed (dotted lines) there is insufficient power for the geodynamo for 700 Myrs prior to inner core nucleation. Once the inner core forms precipitation rate is low in both cases and changes in oxygen concentration are primarily driven by inner core growth.

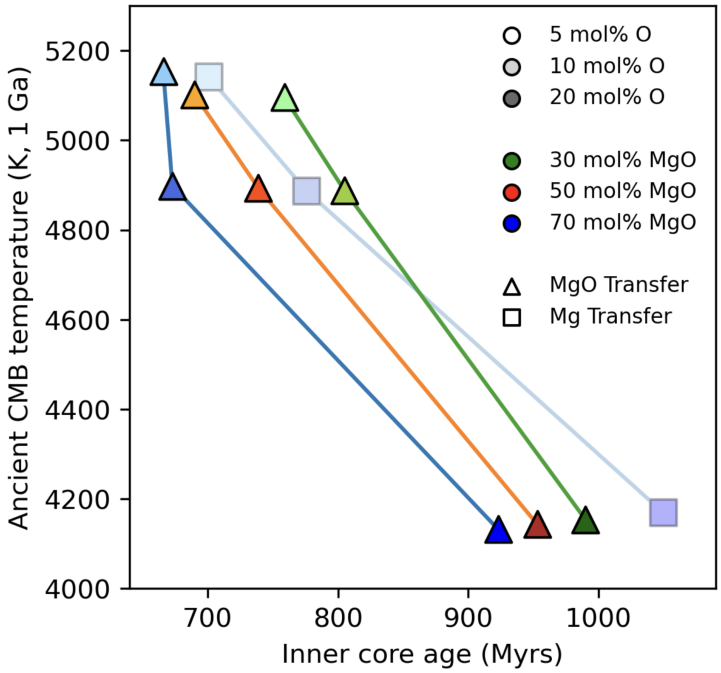

Figure 4: Inner core age and CMB temperature at 1 Ga for thermal histories including the precipitation of Mg from the liquid core. Initial oxygen content of 5, 10 and 20 mol. % are shown as light, medium and dark colours respectively. Mantle compositions with 30 (greens), 50 (reds, pyrolitic) and 70 (blues) mol. % MgO are compared. Cases where Mg and O are extracted from the core in equal proportion (triangles) produce $E_j > 0$ prior to inner core formation (solid colours) whereas cases where only Mg is removed to the mantle (squares) do not (transparent colours).

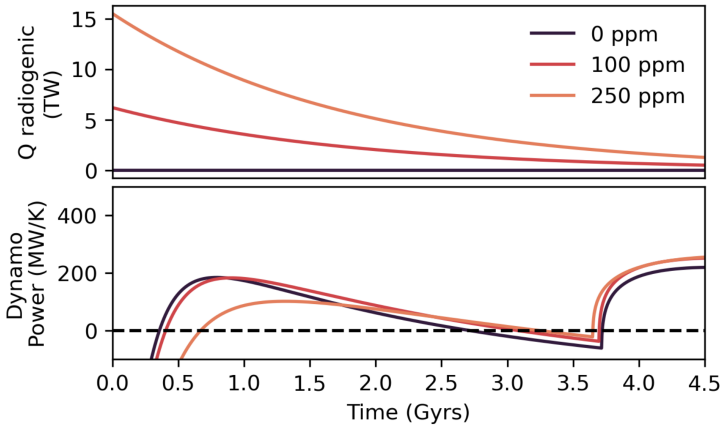

Figure 5: Radiogenic power in the core from decay of ^{40}K for parameterised thermal evolution models. Thermal histories are shown with initial ^{40}K concentrations of 0 (black), 100 (red) and 250 ppm (orange) which corresponds to the equilibrium concentration at the CMB for a temperature of 5500 K, as an upper limit case.

Badro et al., 2015; Davies et al., 2015). Power is integrated into our model assuming 2.6×10^{-15} W kg^{-1} ppm^{-1} (Clauser and Gupta, 2011). The temperature and E_j of the core are extremely similar across all of these cases with even the highest concentration only contributing 1.3 TW at the present day. Decay of ^{40}K is, even in the most optimistic case, just short of providing the required power to sustain the geodynamo prior to inner core nucleation. This agrees with the findings of (Driscoll and Davies, 2023) who found that a present day radiogenic heat production of ≥ 2 TW and an $f_{viscosity} \leq 10$ (3-8 in our cases) is needed for $E_j > 0$ prior to inner core formation and a present day inner core radius of 1221 km.

5. Conclusions

In this work we have calculated the solubility of MgO and K_2O in liquid Fe mixtures representative of Earth's core composition and in equilibrium with both a solid oxide and liquid silicates representative of an early magma ocean, at times when the bottom of the mantle may have been completely molten. The methods used are similar to those we previously employed to investigate FeO solubility (see Pozzo et al., 2019), with solubility data here determined by computing the chemical potentials of MgO and K_2O at high P, T and variable composition in liquid Fe mixtures and silicate solids and melts. Our results, in addition to previous implementations of these methods (Pozzo et al., 2019; Wilson et al., 2022), show that this approach of calculating K_D from ab initio simulations is consistent with experimental studies of metal-silicate partitioning at high pressure and temperature.

By computing chemical potentials we have established that K_D^K for the core is small. These results are consistent with those of Xiong et al. (2018), although implementing different reactions mean a $\sim$10$\times$ greater concentration in the core here compared to the previous study. The highest concentration of K in the core that our results can justify remains small, only 250 ppm, contributing less than 2 TW of power to the present day core (see also Pozzo et al., 2022). Our most optimistic case fails to maintain positive entropy for the geodynamo prior to inner core formation. This finding is in line with those of Nimmo et al. (2004) who also found that high k thermal histories with less than 400 ppm of K in the core could not maintain $E_j > 0$. The

influence of ^{40}K on the thermal evolution of the core is therefore important, but unable to sustain the geodynamo alone. The reaction by which K is exchanged with the mantle is of greater importance than the specific value of K_D^K, which is agreed to be small.

We find that low concentrations of Mg can be stable in the liquid core, consistent with Wahl and Militzer (2015). Our results of K_D^{Mg} agree with the model of Badro et al. (2018), which we use to define the precipitation in our thermal histories. The precipitation rates in these histories are predictably similar to those found by Badro et al. (2018) and are also similar O'Rourke and Stevenson (2016). Du et al. (2017) find a lower temperature dependence of Mg solubility, leading to the conclusion that substantial secular cooling is needed in combination with Mg precipitation to drive the geodynamo. Despite our results giving more convective power, we find that there is insufficient Mg dissolved into the early core to consistently sustain the geodynamo through precipitation. However, if Mg is removed from the core as MgO the O dependence of Mg solubility increases the overall precipitation rate and is capable of maintaining $E_j > 0$ prior to inner core formation. Based on these findings, it is most pertinent to understand the exact mechanisms of multi-element precipitation from the core, as individual elements and mechanisms are thus far unable to unambiguously resolve the new core paradox alone.

Acknowledgements

We acknowledge a Natural Environment Research Council grant, reference NE/T000228/1, which supports all authors on this project. DA and MP acknowledge support from the Natural Environment Research Council (NERC) grant numbers NE/M000990/1 and NE/R000425/1. Calculations were performed on the Monsoon2 system, a collaborative facility supplied under the Joint Weather and Climate Research Programme, a strategic partnership between the UK Met Office and NERC. Calculations were also performed at University College London (UCL) Research Computing, on the MMM hub EP/P020194/1, on the Oak Ridge Leadership Computing Facility (DE-AC05-00OR22725), on the cluster HPC IBiSCo at Università di Napoli Federico II, Instituto Nazionale per la Fisica Nucleare and Consiglio Nazionale per le Ricerche, funded by project code PIR01_00011 IBiSCo, PON 2014-2020 and on the UK national supercomputer facility Archer2, also funded by NERC grant, reference NE/T000228/1.

References

Alfe, D., 1999. Ab initio molecular dynamics, a simple algorithm for charge extrapolation. Computer Physics Communications 118, 31–33.

Alfè, D., 2009. Phon: A program to calculate phonons using the small displacement method. Computer Physics Communications 180, 2622–2633.

Badro, J., Aubert, J., Hirose, K., Nomura, R., Blanchard, I., Borensztajn,

S., Siebert, J., 2018. Magnesium partitioning between Earth's mantle and core and its potential to drive an early exsolution geodynamo. Geophysical Research Letters 45, 13–240.

Badro, J., Brodholt, J.P., Piet, H., Siebert, J., Ryerson, F.J., 2015. Core formation and core composition from coupled geochemical and geophysical constraints. Proceedings of the National Academy of Sciences 112, 12310–12314.

Badro, J., Siebert, J., Nimmo, F., 2016. An early geodynamo driven by exsolution of mantle components from Earth's core. Nature 536, 326–328.

Biggin, A.J., de Wit, M.J., Langereis, C.G., Zegers, T.E., Voûte, S., Dekkers, M.J., Drost, K., 2011. Palaeomagnetism of archaean rocks of the onverwacht group, barberton greenstone belt (southern africa): Evidence for a stable and potentially reversing geomagnetic field at ca. 3.5 ga. Earth and Planetary Science Letters 302, 314–328.

Blanchard, I., Siebert, J., Borensztajn, S., Badro, J., 2017. The solubility of heat-producing elements in earth's core. Geochemical Perspectives Letters 5.

Blöchl, P.E., 1994. Projector augmented-wave method. Physical review B 50, 17953.

Bono, R.K., Paterson, G.A., van der Boon, A., Engbers, Y.A., Michael Grappone, J., Handford, B., Hawkins, L.M., Lloyd, S.J., Sprain, C.J., Thallner,

D., et al., 2022. The pint database: a definitive compilation of absolute palaeomagnetic intensity determinations since 4 billion years ago. Geophysical Journal International 229, 522–545.

Bouhifd, M.A., Gautron, L., Bolfan-Casanova, N., Malavergne, V., Hammouda, T., Andrault, D., Jephcoat, A., 2007. Potassium partitioning into molten iron alloys at high-pressure: Implications for earth's core. Physics of the Earth and Planetary Interiors 160, 22–33.

Chidester, B.A., Rahman, Z., Righter, K., Campbell, A.J., 2017. Metal–silicate partitioning of u: Implications for the heat budget of the core and evidence for reduced u in the mantle. Geochimica et Cosmochimica Acta 199, 1–12.

Clauser, C., Gupta, H., 2011. Radiogenic heat production of rocks. Encyclopedia of solid earth geophysics 2, 1–11.

Davies, C., 2015. Cooling history of Earth's core with high thermal conductivity. Physics of the Earth and Planetary Interiors 247, 65–79.

Davies, C., Greenwood, S., 2023. Thermo-chemical dynamics in Earth's core arising from interactions with the mantle. eartharxiv.org 0, 0.

Davies, C., Pozzo, M., Gubbins, D., Alfè, D., 2015. Constraints from material properties on the dynamics and evolution of Earth's core. Nature Geoscience 8, 678–685.

Driscoll, P., Bercovici, D., 2014. On the thermal and magnetic histories of Earth and Venus: Influences of melting, radioactivity, and conductivity. Physics of the Earth and Planetary Interiors 236, 36–51.

Driscoll, P., Davies, C., 2023. The "new core paradox:" challenges and potential solutions. Journal of Geophysical Research: Solid Earth , e2022JB025355.

Du, Z., Boujibar, A., Driscoll, P., Fei, Y., 2019. Experimental constraints on an mgo exsolution-driven geodynamo. Geophysical Research Letters 46, 7379–7385.

Du, Z., Jackson, C., Bennett, N., Driscoll, P., Deng, J., Lee, K.K., Greenberg, E., Prakapenka, V.B., Fei, Y., 2017. Insufficient energy from MgO exsolution to power early geodynamo. Geophysical Research Letters 44, 11–376.

Fischer, R.A., Nakajima, Y., Campbell, A.J., Frost, D.J., Harries, D., Langenhorst, F., Miyajima, N., Pollok, K., Rubie, D.C., 2015. High pressure metal–silicate partitioning of Ni, Co, V, Cr, Si, and O. Geochimica et Cosmochimica Acta 167, 177–194.

Fu, R.R., Drabon, N., Wiedenbeck, M., Brenner, A.R., Lowe, D.R., Borlina, C.S., 2021. Paleomagnetism of 3.5-4.0 ga zircons from the barberton greenstone belt, south africa. Earth and Planetary Science Letters 567, 116999.

Gessmann, C., Wood, B., 2002. Potassium in the earth's core? Earth and Planetary Science Letters 200, 63–78.

Gomi, H., Ohta, K., Hirose, K., Labrosse, S., Caracas, R., Verstraete, M.J., Hernlund, J.W., 2013. The high conductivity of iron and thermal evolution of the Earth's core. Physics of the Earth and Planetary Interiors 224, 88–103.

Greenwood, S., Davies, C., Mound, J., 2021. On the evolution of thermally stratified layers at the top of Earth's core. Physics of the Earth and Planetary Interiors , 106763.

Helffrich, G., Hirose, K., Nomura, R., 2020. Thermodynamical modeling of liquid Fe-Si-Mg-O: Molten magnesium silicate release from the core. Geophysical Research Letters 47, e2020GL089218.

Hirao, N., Ohtani, E., Kondo, T., Endo, N., Kuba, T., Suzuki, T., Kikegawa, T., 2006. Partitioning of potassium between iron and silicate at the core-mantle boundary. Geophysical research letters 33.

Hohenberg, P., Kohn, W., 1964. Inhomogeneous electron gas. Physical review 136, B864.

Inoue, H., Suehiro, S., Ohta, K., Hirose, K., Ohishi, Y., 2020. Resistivity saturation of hcp fe-si alloys in an internally heated diamond anvil cell: A key to assessing the earth's core conductivity. Earth and Planetary Science Letters 543, 116357.

Jackson, C.R., Bennett, N.R., Du, Z., Cottrell, E., Fei, Y., 2018. Early episodes of high-pressure core formation preserved in plume mantle. Nature 553, 491–495.

Jaupart, C., Labrosse, S., Lucazeau, F., Mareschal, J., 2007. 7.06-temperatures, heat and energy in the mantle of the earth. Treatise on geophysics 7, 223–270.

Katsura, T., Yoneda, A., Yamazaki, D., Yoshino, T., Ito, E., 2010. Adiabatic temperature profile in the mantle. Physics of the Earth and Planetary Interiors 183, 212–218.

Kohn, W., Sham, L.J., 1965. Self-consistent equations including exchange and correlation effects. Physical review 140, A1133.

de Koker, N., Steinle-Neumann, G., Vlček, V., 2012. Electrical resistivity and thermal conductivity of liquid Fe alloys at high P and T, and heat flux in Earth's core. Proceedings of the National Academy of Sciences 109, 4070–4073.

Kresse, G., Furthmüller, J., 1996. Efficient iterative schemes for ab initio total-energy calculations using a plane-wave basis set. Physical review B 54, 11169.

Kresse, G., Joubert, D., 1999. From ultrasoft pseudopotentials to the projector augmented-wave method. Physical review b 59, 1758.

Labrosse, S., 2015. Thermal evolution of the core with a high thermal conductivity. Physics of the Earth and Planetary Interiors 247, 36–55.

Ma, Z., 2001. Thermodynamic description for concentrated metallic solutions using interaction parameters. Metallurgical and Materials Transactions B 32, 87–103.

McDonough, W.F., Sun, S.S., 1995. The composition of the earth. Chemical geology 120, 223–253.

Mittal, T., Knezek, N., Arveson, S.M., McGuire, C.P., Williams, C.D., Jones, T.D., Li, J., 2020. Precipitation of multiple light elements to power Earth's early dynamo. Earth and Planetary Science Letters 532, 116030.

Murthy, V.R., Van Westrenen, W., Fei, Y., 2003. Experimental evidence that potassium is a substantial radioactive heat source in planetary cores. Nature 423, 163–165.

Nakagawa, T., Tackley, P.J., 2010. Influence of initial cmb temperature and other parameters on the thermal evolution of earth's core resulting from thermochemical spherical mantle convection. Geochemistry, Geophysics, Geosystems 11.

Nimmo, F., 2015a. Energetics of the core, in: Schubert, G. (Ed.), Treatise on geophysics 2nd Edn. Elsevier, Amsterdam. volume 8, p. 27–55.

Nimmo, F., 2015b. Energetics of the core, in: Schubert, G. (Ed.), Treatise on Geophysics 2nd Edn, Vol. 8. Elsevier, Amsterdam, pp. 27–55.

Nimmo, F., Price, G., Brodholt, J., Gubbins, D., 2004. The influence of potassium on core and geodynamo evolution. Geophysical Journal International 156, 363–376.

Nosé, S., 1984. A unified formulation of the constant temperature molecular dynamics methods. The Journal of chemical physics 81, 511–519.

Ohta, K., Kuwayama, Y., Hirose, K., Shimizu, K., Ohishi, Y., 2016. Experimental determination of the electrical resistivity of iron at earth's core conditions. Nature 534, 95–98.

O'Rourke, J.G., Korenaga, J., Stevenson, D.J., 2017. Thermal evolution of earth with magnesium precipitation in the core. Earth and Planetary Science Letters 458, 263–272.

O'Rourke, J.G., Stevenson, D.J., 2016. Powering Earth's dynamo with magnesium precipitation from the core. Nature 529, 387–389.

Pourovskii, L., Mravlje, J., Pozzo, M., Alfe, D., 2020. Electronic correlations and transport in iron at earth's core conditions. Nature communications 11, 4105.

Pozzo, M., Davies, C., Gubbins, D., Alfè, D., 2012. Thermal and electrical conductivity of iron at Earth's core conditions. Nature 485, 355–358.

Pozzo, M., Davies, C., Gubbins, D., Alfe, D., 2013. Transport properties for liquid silicon-oxygen-iron mixtures at earth's core conditions. Physical Review B 87, 014110.

Pozzo, M., Davies, C., Gubbins, D., Alfè, D., 2014. Thermal and electrical conductivity of solid iron and iron–silicon mixtures at earth's core conditions. Earth and Planetary Science Letters 393, 159–164.

Pozzo, M., Davies, C.J., Alfè, D., 2022. Towards reconciling experimental and computational determinations of earth's core thermal conductivity. Earth and Planetary Science Letters 584, 117466.

Pozzo, M., Davies, C.J., Gubbins, D., Alfe, D., 2019. FeO content of Earth's liquid core. Physical Review X 9, 041018.

Rubie, D.C., Jacobson, S.A., Morbidelli, A., O'Brien, D.P., Young, E.D., de Vries, J., Nimmo, F., Palme, H., Frost, D.J., 2015. Accretion and differentiation of the terrestrial planets with implications for the compositions of early-formed solar system bodies and accretion of water. Icarus 248, 89–108.

Stacey, F., Loper, D., 2007. A revised estimate of the conductivity of iron alloy at high pressure and implications for the core energy balance. Physics of the Earth and Planetary Interiors 161, 13–18.

Stacey, F.D., Anderson, O.L., 2001. Electrical and thermal conductivities of fe–ni–si alloy under core conditions. Physics of the Earth and Planetary Interiors 124, 153–162.

Tarduno, J.A., Cottrell, R.D., Bono, R.K., Oda, H., Davis, W.J., Fayek, M., Erve, O.v., Nimmo, F., Huang, W., Thern, E.R., et al., 2020. Pale-

omagnetism indicates that primary magnetite in zircon records a strong hadean geodynamo. Proceedings of the National Academy of Sciences 117, 2309–2318.

Tarduno, J.A., Cottrell, R.D., Davis, W.J., Nimmo, F., Bono, R.K., 2015. A hadean to paleoarchean geodynamo recorded by single zircon crystals. Science 349, 521–524.

Wahl, S.M., Militzer, B., 2015. High-temperature miscibility of iron and rock during terrestrial planet formation. Earth and Planetary Science Letters 410, 25–33.

Wang, Y., Perdew, J.P., 1991. Correlation hole of the spin-polarized electron gas, with exact small-wave-vector and high-density scaling. Physical Review B 44, 13298.

Watanabe, K., Ohtani, E., Kamada, S., Sakamaki, T., Miyahara, M., Ito, Y., 2014. The abundance of potassium in the earth's core. Physics of the Earth and Planetary Interiors 237, 65–72.

Wilson, A.J., Pozzo, M., Alfè, D., Walker, A.M., Greenwood, S., Pommier, A., Davies, C.J., 2022. Powering earth's ancient dynamo with silicon precipitation. Geophysical Research Letters 49, e2022GL100692.

Wohlers, A., Wood, B.J., 2015. A mercury-like component of early earth yields uranium in the core and high mantle 142nd. Nature 520, 337–340.

Xiong, Z., Tsuchiya, T., Taniuchi, T., 2018. Ab initio prediction of potassium partitioning into earth's core. Journal of Geophysical Research: Solid Earth 123, 6451–6458.

Zhang, Y., Luo, K., Hou, M., Driscoll, P., Salke, N.P., Minár, J., Prakapenka, V.B., Greenberg, E., Hemley, R.J., Cohen, R., et al., 2022. Thermal conductivity of fe-si alloys and thermal stratification in earth's core. Proceedings of the National Academy of Sciences 119.